

Trabalho de Conclusão de Curso

Emergent electronic states on the Dirac semimetal NiTe₂

Rodrigo Tardini Paulino^{1,*}

¹*Centro de Ciências Naturais e Humanas,*

Universidade Federal do ABC, Santo André-SP, Brasil

In this graduation thesis, the single-crystalline growth and systematic study of the type-II Dirac semimetal NiTe₂ was performed. The crystalline phase was determined by means of powder X-ray diffraction, as well as the highly metallic character of its charge carriers from resistivity measurements and from the dominant Pauli paramagnetism of the itinerant electrons. Most importantly, the Fermi surface of this topological material was indirectly probed through the de Haas-van Alphen effect, where two different oscillations were resolved, signaling the presence of at least two conducting bands at the Fermi level. The charge carriers were found to have very low effective masses of 0.13(3) m_0 and 0.20(4) m_0 , where m_0 is the free electron mass, and the topological character of the bands was found to be non-trivial from the Berry phase of the oscillations.

1. INTRODUCTION

Following the groundbreaking graphene experiments performed by Novoselov and Geim in 2005 [1], a new field in condensed matter physics emerged, focused on studying how conducting states could appear in a material that would normally be an insulator. Kane *et al.* showed that while the valence and conducting bands are separated by a bulk energy gap in these so-called topological insulators, the band topology and the crystalline symmetry requires that the bands touch at a single point in momentum space, corresponding to the edge of the material. Furthermore, theoretical results showed that the charge carriers followed a linear dispersing relation, typical of relativistic particles, where the bands came in contact

*Electronic address: rodrigo.paulino@ufabc.edu.br

through a cone-like structure named as a Dirac cone [2, 3]. The prediction of perturbation-protected edge states naturally gained the attention of several different areas of research (ranging from spintronics to quantum information), and the search for new topological materials became of great interest to the academic community[4].

It was found that this topological phase was not restricted to 2D materials, such as graphene or HgTe/CdTe quantum well structures [5], but had a three dimensional counterpart where the Dirac cone presented protected surface states and a locking between spin and momentum. Experimentally, the first generation of 3D topological insulators was established by the semiconducting alloys in the $\text{Bi}_{1-x}\text{Sb}_x$ family [6], but it was later joined by the "second generation materials" Bi_2Se_3 , Bi_2Te_3 and Sb_2Te_3 , presenting a larger bulk band gap that enables further exploration of the topological effects [7].

Since then, the classification of materials based on their topological properties extended to metals, semimetals and even superconductors. As an example, a Weyl Semimetal (WSM) presents linear dispersion in all 3 dimensions with 3D-Dirac (or Weyl) "cones". A point in the Brillouin zone (BZ) where this band crossing occurs is named a Weyl node, and these act as sources (or sinks) of the so-called Berry field¹, depending on their chirality. Since the net chirality of a BZ is required to be null, Weyl nodes must always come in pairs [8]. Experimental examples are TaAs [9], the transition-metal pnictide family [10] and the Kagomé crystal Co_2MnGa [11].

If both time-reversal and inversion symmetry are present, the pair of Weyl nodes may merge and a single non-chiral Dirac cone appears, with a 4-fold degeneracy at the crossing. This is the Dirac Semimetal (DSM) phase, and is sometimes considered as a 3D version of graphene. The merging of the Weyl nodes is hard to realize experimentally because it is only guaranteed from crystalline symmetry (not the topology), but several such materials have been found over the last decade. Examples are Cd_3As_2 [12] and the A_3Bi_2 family ($\text{A}=\text{Na},\text{K},\text{Rb}$)[13].

In 2015, Soluyanov *et al.* [14] described a new topological phase that hosted a novel type of fermion, not predicted earlier in the context of high-energy physics because it breaks the Lorentz invariance of the Dirac equation, contrary to Dirac, Weyl or even Majorana

¹ The Berry field is mathematically similar to the regular magnetic field, with the main difference coming from the existence of Weyl nodes, that act as monopoles of the Berry flux. See [8].

fermions². These so-called type-II Weyl semimetals present Weyl cones that are tilted in a specific direction. In contrast to regular (type-I) WSM that possess closed (usually spherical) Fermi surfaces, type-II WSM can present an open Fermi surface with contact points between hole and electron pockets. Several realizations of these anisotropic materials have been realized, such as MoTe₂ [15] and WTe₂ [16].

Combining both concepts above, a type-II Dirac semimetal phase (type-II DSM) hosts a tilted Dirac cone with 4-fold degeneracy. This phase was predicted for the first time in the PtSe₂ system [17, 18], where a pair of strongly tilted Dirac cones appeared at the k_z -axis of the BZ, protected by the structural symmetry of the $P\bar{3}m1$ space group. Practical consequences of the relativistic fermions could not be further explored in this material because the Dirac point is far below the Fermi level. The related compound NiTe₂ was predicted in 2018 by Xu *et al.* to host type-II Dirac fermions just above the Fermi energy [19], where direct consequences of these relativistic charge carriers appeared in the large linear magnetoresistance and in the quantum oscillations of the magnetization. The topological phase of the material was confirmed by Ghosh *et al.* [20] and subsequently in 2020 by Mukherjee *et al.* [21]. As a possible consequences of the topology, superconducting phases have also been predicted down to the monolayer limit [22, 23], under hydrostatic pressure [24] and through chemical doping [25–27].

In general, the topological character of a material can only be fully determined experimentally through the direct observation of the Fermi surface structure, using angle-resolved photoemission spectroscopy (ARPES). But the sophisticated nature of this method invites the use of simpler and/or indirect probes of the Fermi surface, such as quantum oscillations that are manifested under applied magnetic fields in certain circumstances. Fundamentally, these oscillations arise from periodical changes in the density of states available as the Landau levels (LLs) cross the Fermi level, as a function the inverse of the magnetic field. Such effect has consequences in several properties of metals, such as the magnetoresistivity (Shubnikov-de Haas oscillations), Hall resistivity, thermoelectric power and, most directly, in the magnetization, in the form of the de Haas-van Alphen effect, that will be discussed in detail in Section 2. In topologically non-trivial materials, the charge carriers gain an additional geometrical (Berry) phase as they go into the cyclotron orbits of the LLs, re-

² A Majorana fermion is predicted to appear at each edge state of a 2D topological insulator [4]

maintaining one of the few direct observations of relativistic fermions available through a simple experimental procedure.

In this undergraduate thesis, the experimental characterization of the type-II Dirac semimetal NiTe₂ was performed. Starting with the single crystal growth and structural characterization, the electronic and magnetic responses were then studied through resistivity, magnetization and, finally, through measurements of the de Haas-van Alphen effect. The experiments are detailed in Section 3 and the analysis of the results are thoroughly discussed in Section 4. The work performed is based on the article by Xu *et al.* [19], with a few important differences outlined in the discussion and the conclusion.

2. THE DE HAAS-VAN ALPHEN EFFECT

This chapter aims to present an intuitive theoretical understanding of the oscillations in the magnetization observed experimentally by W.J. de Haas and P.M. van Alphen in 1930 when studying the magnetism of bismuth [28]. Subsection 2.1 starts from Landau's solution of the confined electron under a constant magnetic field [29] [30], following on subsection 2.2 with an explanation of the oscillatory behaviour as a function of the applied magnetic field. The last part of this chapter addresses the generalizations made by Onsager for the electron in a periodic potential [31] and the general formula considering temperature damping, known as the Lifshitz-Kosevich formula [32], [33]. CGS gaussian units are used in this derivation.

2.1. Landau levels in free electrons

In order to understand the full phenomena, let's first take a closer look on the simpler case of free non-relativistic electrons under a constant magnetic field \mathbf{H} . We set to write the Hamiltonian \mathcal{H} of an electron of charge $-e$ and intrinsic magnetic dipole moment $\hat{\mu}$, under a magnetic field.

Just as in classical physics, we can perform the minimal coupling of a free particle to a magnetic field by substituting $\hat{\mathbf{p}} \rightarrow \hat{\mathbf{p}} + q\mathbf{A}/c$, where $\hat{\mathbf{A}}$ is the operator related to the vector potential of the magnetic field and q the particle's electric charge. Next, we consider the coupling of the electron spin to the field by subtracting $\hat{\mu} \cdot \mathbf{H}$ to the Hamiltonian:

$$\mathcal{H} = \frac{(\hat{\mathbf{p}} - e\mathbf{A}/c)^2}{2m} - \hat{\boldsymbol{\mu}} \cdot H. \quad (1)$$

Using the Bohr magneton ($\mu_B = e\hbar/2m_e c = 0.927 \times 10^{-20}$ erg/gauss) and the spin g_s -factor of $g_s \approx 2$ for the electron, the intrinsic magnetic moment can be rewritten as $\hat{\boldsymbol{\mu}} = -g_s \mu_B \hat{\mathbf{S}}/\hbar$, where $\hat{\mathbf{S}}$ is the spin operator of projected eigenvalues $s_z = \pm\hbar/2$.

In order to determine what are the energy levels of these particles, we can orient the magnetic field on the \hat{z} direction and, using the gauge invariance of the magnetic field, the vector potential operator is taken to be $\mathbf{A} = -Hy\hat{\mathbf{x}}$. The hamiltonian becomes

$$\mathcal{H} = \frac{1}{2m} \left(\hat{p}_x + \frac{eHy}{c} \right)^2 + \frac{\hat{p}_y^2}{2m} + \frac{\hat{p}_z^2}{2m} + \frac{g_s \mu_B}{\hbar} \hat{s}_z H. \quad (2)$$

Since it doesn't have \hat{s}_x or \hat{s}_y terms, the hamiltonian commutes with the \hat{s}_z operator. The same is valid for \hat{p}_x (\hat{p}_z) because \hat{x} (\hat{z}) is not present. Therefore, these are all conserved quantities.

As a consequence, the total wave function can be taken as an eigenstate of the spin operator \hat{s}_z with eigenvalue s_z , and we can write Schrodinger's equation for the spatial wave function ψ as

$$\frac{1}{2m} \left[\left(\hat{p}_x + \frac{eHy}{c} \right)^2 + \hat{p}_y^2 + \hat{p}_z^2 \right] \psi + \frac{g_s \mu_B}{\hbar} s_z H \psi = \epsilon \psi \quad (3)$$

with \hat{p}_x and \hat{p}_z as conserved quantities, we can use separation of variables to show that the eigenfunction we look for is in the form

$$\psi = \chi(y) e^{\frac{i}{\hbar}(xp_x + zp_z)}. \quad (4)$$

Substituting back into Schrodinger's equation, considering the momentum operator in coordinate space $\hat{\mathbf{p}} = -i\hbar\nabla$, we obtain the ODE

$$\chi'' + \frac{2m}{\hbar^2} \left[\epsilon - \frac{g_s \mu_B}{\hbar} s_z H - \frac{p_z^2}{2m} - \frac{1}{2} m \omega_H^2 (y - y_0)^2 \right] \chi = 0, \quad (5)$$

where the frequency is $\omega_H = \frac{eH}{mc}$ and the central coordinate on the y direction is $y_0 = \frac{-cp_x}{eH}$. The deduction of this result is in Appendix A 1.

We can readily see that this ODE is formally identical to that of the quantum harmonic oscillator, with the addition of the spin and the free momentum in the z direction. The energy is then

$$\epsilon(n, k_z) = \frac{\hbar^2 k_z^2}{2m} + \hbar\omega_H \left(n + \frac{1}{2} \right) + \frac{g_s \mu_B}{\hbar} s_z H, \quad (6)$$

$$= \frac{\hbar^2 k_z^2}{2m} + \hbar\omega_H \left(n + \frac{1}{2} + \sigma \right), \quad (7)$$

where $\sigma = \pm 1$ depending on the spin eigenvalue. Note that the free particle, otherwise having a continuum energy spectrum, becomes quantized under a magnetic field. The states with a given value of the discrete quantum number n are known as Landau levels, and the energy spacing of each Landau level $\hbar\omega_H$ increases linearly with H .

The eigenfunction can be taken from the harmonic oscillator solution to be

$$\chi_n(y) = \frac{1}{\sqrt{\pi^{1/2} a_H (2^n n!)}} \exp\left[-\frac{(y - y_0)^2}{2a_H^2}\right] H_n\left(\frac{y - y_0}{a_H}\right) \quad (8)$$

with $a_H = \sqrt{\frac{\hbar}{m\omega_H}}$ and H_n as the Hermite polynomials of order n .

This eigenstate can be looked at as a similar form to the classical picture of the cyclotron orbit of the electron, where the momentum in the direction of the field can take any value, and the electron has a ‘‘circular orbit’’ on the xy plane with the cyclotron frequency $\omega_H = \frac{eH}{mc}$ and central coordinates $(x_0, y_0) = (\frac{cp_y}{eH}, \frac{-cp_x}{eH})^3$. Since the z -coordinate is not influenced by the field, the semi-classical orbit of the electron has a cylindrical form, called the Landau tube.

The next step is to determine the degeneracy of each Landau level. For this, consider the electron at its fundamental state, confined in a box of size L_x , L_y and L_z . By applying the boundary conditions on the wave function (Eq. 4), the wave number becomes quantized as

$$k_x = \frac{2\pi}{L_x} m, \quad (9)$$

where m is an integer quantum number. The value of m is further restricted when you consider $y_0 = \frac{c\hbar k_x}{eH}$, that can be thought as the y -coordinate for the center of the oscillatory wave function. The center must physically lie within the system ($0 \leq y_0 < L_y$) resulting in

$$k_x < \frac{eHL_y}{c\hbar}. \quad (10)$$

³ x_0 can be shown to be a conserved quantity as well and is the constant that appears in the place of y_0 , when the problem is solved using another gauge, with the magnetic potential vector $\mathbf{A} = Hx\hat{y}$ for the magnetic field instead of $\mathbf{A} = -Hy\hat{x}$

Combining both results:

$$0 \leq m < \frac{eHL_xL_y}{2\pi c\hbar}. \quad (11)$$

The degeneracy of the Landau levels is given by the maximum value of m ,

$$\eta = \frac{AH}{\phi_0}, \quad (12)$$

where H is the field, $\phi_0 = \frac{hc}{2e}$ is the flux quanta, and A is the area of the box.

Notice that the degeneracy of the Landau levels increases with applied field. This effect, combined with the energy spacing increase, will lead to an oscillatory behaviour on the internal energy of a multiparticle system, and is the origin of the de Haas-van Alphen oscillations.

2.2. The periodicity of the oscillations

In a system of N non-interacting electrons, when a magnetic field is applied, the levels $n = 0, 1, 2, \dots, k - 1$ will be fully occupied with η electrons each, while the level $n = k$ will be partially occupied with $\lambda\eta$ electrons. Thus we have $N = \eta(k + \lambda)$ electrons, and using Eq. 12

$$k + \lambda = \frac{N\phi_0}{A} \frac{1}{H} \equiv \frac{H_0}{H}, \quad (13)$$

where $H_0 = \frac{N\phi_0}{A}$ is the minimum field required to put all the electrons in the lowest Landau level ($k = 0$).

Notice that k has an integer value and $\lambda \in [0, 1)$, so we can define

$$k = \left[\frac{H_0}{H} \right], \quad \lambda = \frac{H_0}{H} - \left[\frac{H_0}{H} \right], \quad (14)$$

where $[x]$ represents the integer value of x , rounded down.

The energy of the entire system is obtained simply by summing over the energies of individual electrons. By taking Eq. 6, considering $k_z = 0$ and that the overall contribution of spin is cancelled out, we get

$$E(H) = \eta\hbar\omega_H \left[\sum_{n=0}^{k-1} \left(n + \frac{1}{2} \right) + \left(k + \frac{1}{2} \right) \lambda \right], \quad (15)$$

that can be further simplified to (details in Appendix A 2)

$$E(H) = \frac{N^2 \pi \hbar^2}{2mA} + \frac{N \hbar \omega_H}{2(k + \lambda)} \lambda (1 - \lambda), \quad (16)$$

and, considering that the energy at null magnetic field and temperature is

$$E(H = 0) = \frac{N^2 \pi \hbar^2}{A 2m}, \quad (17)$$

the energy can be represented in the much simpler form

$$\frac{E(H)}{E(H = 0)} = 1 + \left(\frac{H}{H_0} \right)^2 \lambda (1 - \lambda). \quad (18)$$

From equation 18, it can be seen that the energy of the system increases with H^2 and, most importantly, Eq. 14 shows that the filling of the last occupied Landau level (λ) vanishes when $\frac{H_0}{H}$ is an integer, that happens periodically with $\frac{1}{H}$. The energy will follow that same oscillatory pattern.

Since the magnetization is defined as

$$M = -\frac{\partial E}{\partial H}, \quad (19)$$

then M will also oscillate with a constant period at $\frac{1}{H}$

$$\Delta \left(\frac{1}{H} \right) = \frac{1}{H_0} = \frac{2eA}{hcN}. \quad (20)$$

In order to further simplify this relation, we first need to find the Fermi energy of the free electrons in this closed box. Since the energy eigenvalues are evenly spaced in momentum (see Eq. 9) from $\epsilon = 0$ up to $\epsilon = \epsilon_F$, the system's energy without a magnetic field can be redefined as all N electrons at half the Fermi energy

$$E(H = 0) = \frac{N^2 \pi \hbar^2}{A 2m} \equiv N \frac{\epsilon_F}{2}. \quad (21)$$

With the Fermi momentum defined from $\epsilon_F = \frac{\hbar^2 k_F^2}{2m}$ and the Fermi area $A_f = \pi k_F^2$, the period of oscillation (Eq. 20) can be inverted to result in

$$F = \frac{\hbar c}{2\pi e} A_f, \quad (22)$$

where F is the frequency of oscillation in units of the applied magnetic field (Oe in CGS or A/m in SI).

This area is fixed for a given number of electrons, but the amount of Landau tubes that fit in it changes depending on the applied field. The radius k_p of the semi-classical Landau tube of level p is

$$\frac{\hbar^2 k_p^2}{2m} = \left(p + \frac{1}{2}\right) \hbar \omega_H \Rightarrow k_p^2 = \left(p + \frac{1}{2}\right) \frac{2\pi e H}{\hbar c}, \quad (23)$$

and because of this result, the oscillations can be seen as the “popping out” of the Landau tubes of the Fermi area.

Even though this was deduced for the case of free non-relativistic electrons, Onsager predicted that fermions in metals exhibit the exact same periodicity relation of Eq. 22. In this case, A_f acts as the extremal (inner or outer) areas of the Fermi surface cross-section perpendicular to the applied field, where the dHvA effect can be interpreted as these “poppings” of the Landau tubes in and out of the Fermi surface [31].

The phase of these oscillations will depend on whether the area of the Fermi surface surrounds an electron or a hole pocket [33], or in the case of topological materials, if the Dirac fermions gain an additional Berry phase when going around the cyclotron orbit [34].

2.3. General form of oscillations

While under ideal conditions the Fermi Surface (FS) would be a sharp mathematical object, the FS in reality is split into two different sheets by the Zeeman effect, and broadened from the effects of finite temperature and impurity scattering. As a result, the dHvA oscillation is no longer described by a pure periodic function, but several periodic functions with slightly different frequencies and phases that contribute to generate a single damped oscillation. In fact, these effects pose an enormous challenge to observe the dHvA effect, that can only be observed in very particular situations. In this section, these damping effects and the general form of the oscillation will be discussed, based on the developments described by Shoenberg [33].

A finite temperature introduces an energy of order $k_B T$ to the fermions close to the Fermi surface, requiring a large enough energy difference between the Landau levels. This imposes the need for low temperatures and high magnetic fields to observe the dHvA effect, and

results in the first damping factor

$$R_T = \frac{\alpha T \mu / B}{\sinh(\alpha T \mu / B)}, \quad (24)$$

where $\alpha = 2\pi^2 k_B m_0 / \hbar e$ and $\mu = m^* / m_0$ is the effective mass in units of the free electron mass.

The second damping effect comes directly from the impurities on the crystalline lattice, where the broadening of the energy levels will now be of order \hbar / τ_q , with τ_q as the quantum relaxation time of the charge carriers. The Dingle damping factor is found to be

$$R_D = \exp[-\alpha T_D \mu / B], \quad (25)$$

where the Dingle temperature T_D is a material constant defined by $T_D = \hbar / (2\pi k_B \tau_q)$. It is also possible to find the quantum mobility of the charge carriers $\mu_q = \frac{e\tau_q}{m^*}$.

Finally, the spin reduction factor is a consequence of the lifted spin degeneracy under a magnetic field, from the Zeeman effect. The superposition of the spin up and spin down dHvA oscillations contribute with a constant damping of

$$R_S = \cos\left(\frac{\pi}{2} g \mu\right), \quad (26)$$

where g is the Landé g factor of the total angular momentum.

Combining such effects on a quantum statistics framework, one can determine the free energy and, consequently, the oscillation on the magnetization. This was first developed by Lifshitz-Kosevich in 1956 [32, 33], and further adapted to relativistic fermions [34] and materials with lower dimensions [35]. There are still other damping effects from sample and magnetic inhomogeneities that are not considered relevant to this work. The revised Lifshitz-Kosevich formula is

$$\Delta M \propto \left(\frac{B}{|\frac{\partial^2 A_F}{\partial k^2}|} \right)^\lambda \sum_{r=1}^{\infty} \frac{(-1)^r}{r^{3/2}} R_T R_D R_S \sin \left[2\pi r \left(\frac{F}{B} - \gamma + \delta \right) \right], \quad (27)$$

where $|\frac{\partial^2 A_F}{\partial k^2}|$ is the curvature of the FS and λ is 1/2 (0) for 3D (2D) materials. The dimension dependent phase δ is $\pm \frac{1}{8}$ for 3D surfaces (0 for 2D), the sign depending on whether the area is a minimum or a maximum of the surface. The sum over r represents the different harmonics of the same oscillation, but in these works only a single harmonic is observed ($r = 1$). The phase γ is simply $+\frac{1}{2}$ in regular metals, but charge carriers in topologically non-trivial

Fermi surfaces gain an additional dependence on the geometric Berry phase Φ_B , resulting in $\gamma = \frac{1}{2} - \frac{\Phi_B}{2\pi}$, where $\Phi_B = \pi$ if the Fermi surface area generating the oscillation is directly around the Dirac crossing point. [34, 35]

Finally, Eq. 27 can be further simplified from the considerations above to

$$\Delta M \propto -B^{1/2} R_T R_D R_S \sin \left[2\pi \left(\frac{F}{B} - \gamma + \delta \right) \right]. \quad (28)$$

3. EXPERIMENTAL METHODS

This section aims to explain all the experimental methods used in this work, starting with the flux growth technique used to obtain the single crystals, followed by the characterization methods used to determine the structural phase, the resistivity and magnetic properties of NiTe₂.

Analyses of the results were made using *Python* 3.8 [36], with the *NumPy* [37] package for importing/processing data, *matplotlib* [38] for plotting and finally the *SciPy* [39] package for performing curve fitting, interpolation and the Fast Fourier Transforms (FFT) required for obtaining the dHvA frequencies.

3.1. Single crystal synthesis

Condensed matter physics is often focused on the study of macroscopic manifestation of delicate quantum phenomena, such as superconductivity and magnetism, that requires high quality samples as a starting point for any experimental work in the area. The visualization of such effects are usually highly dependent on the crystallographic direction and might be suppressed by impurities in the lattice, well exemplified in the de Haas-van Alphen effect described in Section 2.

By growing the material in single-crystalline form, extrinsic factors such as impurities, grain boundaries, or secondary phases can be minimized, while enabling the study of orientation dependent properties. This session is aimed at explaining the flux method used for obtaining the NiTe₂ single crystals.

The flux method consists on providing a stable liquid environment for the reagents to be dissolved and later crystallized into the desired phase upon cooling. The flux is often a metallic element with low melting point and few stable compounds formed with the reagents,

but in the case of NiTe_2 , a self-flux method was possible, where Te is not only part of the compound, but is also the flux.

An advantage of flux growths can be easily seen by considering that Ni can be easily dissolved in liquid Te (above Te's melting point at $T_f = 450^\circ\text{C}$), drastically reducing the required growth temperature from Ni's melting point at $T_f = 1455^\circ\text{C}$. The proportion of Te to the other reagents will determine what phase is the most stable thermodynamically [40], and by cooling it slowly from high temperatures, the crystallization will occur in fewer nucleation sites, reducing the number of crystals, but increasing their size and crystallographic purity. The major disadvantage is that the excess reagent can sometimes become impurity layers or pockets trapped inside the single crystal, but the observation of the de Haas-van Alphen effect indicates that this is not the case in our NiTe_2 crystals.

Following Xu *et al.* [19], about 8 g of reagents at a Ni:Te molar proportion of 1:8 (instead of the stoichiometric 1:2 ratio) was used systematically to obtain NiTe_2 crystals. Other proportions, with 90, 92 and 94% of Te were tested, but no significant improvement was found.

The reagents used were all produced by Alfa Aesar [41] with high purity (99.9999% for Te and 99.95% for Ni). After careful weighing, the elements were sealed under vacuum in a quartz tube with some quartz wool on top, that is later be used for separation of the flux and the crystals. The setup can be visualized in Fig. 1a.

This tube is then placed in a box furnace (Fig. 2a) and submitted to a temperature ramp program, represented in Fig. 1b. The mixture is initially heated to 900°C , guaranteeing all the elements are melted into a homogeneous liquid alloy, followed by fast cooling to right above the melting temperature of the compound (700°C for NiTe_2), then crystallization starts upon slow cooling (2°C per hour) through the melting temperature and below. As crystals grow, the composition of the liquid changes and new phases might form. This can be avoided by stopping the temperature ramp still at a hot enough temperature (500°C for NiTe_2), removing the tube from the furnace and placing it upside down in a centrifuge. The quartz wool inside will allow the passing of the liquid flux, separating the solid crystals from the remaining flux. Large plate-like NiTe_2 single crystals were obtained, with size ranging from of about $1 \times 1 \times 0.1$ mm to $10 \times 10 \times 0.5$ mm, as seen in Fig. 1c.

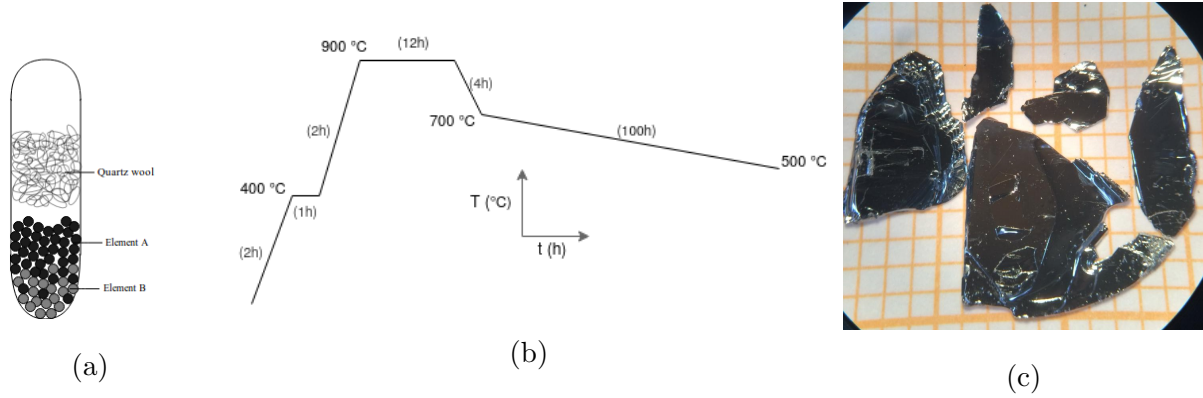


Figure 1: (1a) Diagram of a quartz ampoule, where the reagents are sealed under vacuum and submitted to the temperature ramp. (1b) Temperature ramp used on the single crystalline growth of NiTe_2 . (1c) Single-crystals of NiTe_2 obtained by the self-flux method.

3.2. Structural characterizations

In order to confirm the phase of the grown material, selected single-crystals were crushed into polycrystalline powder with mortar and pestle. The powder X-ray diffraction measurements were performed using a Bruker D2 Phaser (Unicamp) and a Bruker D8 Focus (UFABC Multiuser Central [42]) diffractometers.

Refinement of the diffraction data was performed using the FullProf Suite [43], with the aid of the automatization tool AutoFP [44].

3.3. Electronic transport

In order to measure the NiTe_2 resistivity, the four-probe technique was used in elongated bar-shaped samples cut from the grown single crystals. After cutting the sample surface was cleaned using ultra-fine sand paper (1500 grit and above). Then, four platinum wires of diameter 0.05 mm were placed parallel to each other along the sample surface using silver epoxy (Fig. 3a). The two outer wires pass a uniform current through the sample and the potential difference is measured by the two inner wires. By utilizing a high impedance voltmeter, the intrinsic resistance of the experimental setup can be greatly reduced and, from Ohm's Law ($U = R.I$), the resistivity can be found considering the sample geometry



Figure 2: (2a) Shows the Lindberg Blue M BF51542C Heavy Duty Box Furnace and (2b) the Sorvall Primo 4x100 ml metal cup centrifuge, used on the flux method for single crystalline growth.

$$\rho = \frac{V}{I} \frac{\tau w}{L}, \quad (29)$$

where $\frac{\tau w}{L}$ is the geometrical parameter: τ is the thickness, w is the width and L is the length of the sample. It is worth noting that this assumes a crystal with right angles and a uniform current flow, so the setup has to be prepared with care.

After the samples and contacts are prepared, the other end of the four platinum wires are soldered to an electrical resistivity puck, which is then inserted in a commercial PPMS (Physical Property Measurement System) Evercool 9 by Quantum Design (Fig. 3b), available at the UFABC Multiuser Central [42].

3.4. Magnetic characterization

The de Haas-van Alphen effect requires not only very pure single crystals, but also very sensitive equipment with high magnetic fields and low temperatures. For that matter,

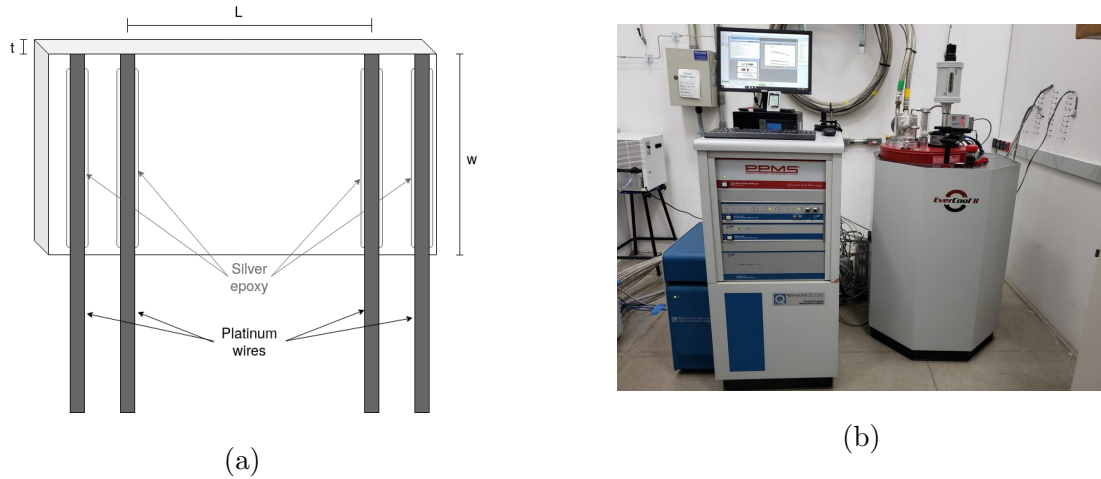


Figure 3: (3a) Representation of a single crystal with the platinum wires used in the 4-probe method (see text). 3b Quantum Design's Evercool 9 PPMS (Physical Property Measurement System), present at the UFABC Multiuser Central.

a Quantum Design MPMS (Magnetic Property Measurement System), equipped with a SQUID (Superconducting Quantum Interferometer Device) sensor, was used for the magnetic experimental studies. The equipment at the UFABC Multiuser Central reaches fields of up to 7 T and temperatures as low as 2 K, enough to observe dHvA oscillations in NiTe_2 .

The VSM (Vibrating Sample Magnetometer) option used measures the sample magnetic moment (M) by vibrating it at a specified frequency at the center of the device sensors, thus altering the induction field ($B = H + 4\pi M$). The oscillating value of the magnetization field will generate an alternating current on the SQUID, allowing it to measure magnetic moments as low as 10^{-7} emu.



Figure 4: Quantum Design MPMS present at the UFABC Multiuser Central [42].

Since NiTe_2 samples usually have a relatively low magnetic moment ($10^{-5} - 10^{-6}$ emu), and the de Haas-van Alphen effect is a collective phenomena, it is better to measure several stacked sheets of the material (about 30 mg) rather than few-layer cleaved surfaces. Some Te from the flux might be present, but its diamagnetic response does not affect the oscillations and can be removed later with data processing.

The method used to insert the sample in the MPMS depends on which crystallographic direction is meant to be parallel to the applied magnetic field (H). For $H \parallel ab$, the single-crystal is attached to the surface of a plastic straw (cut to be 66 mm long) using a bit of vacuum grease, and secured by wrapping the whole setup with another plastic straw cut in the axial direction. Kapton tape is used to ensure the outer straw won't move, and small circular holes are made far from the sample to allow proper venting. For $H \parallel c$, the sample is placed inside the plastic straw, fastened between two folded straw pieces. These setups are illustrated in Fig. 5.

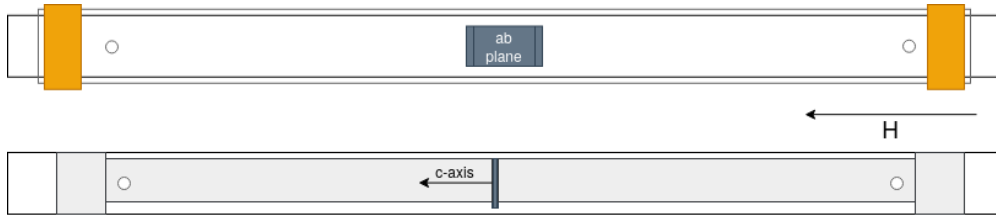


Figure 5: Representation of the straw sample holders used in the MPMS for magnetic measurements. The upper straw is the setup used for $H \parallel ab$ and the lower one is used for $H \parallel c$. The dark grey rectangle represents the planar material, the orange on the sides are the Kapton tape.

In this work, only the de Haas-van Alphen effect with $H \parallel c$ will be studied, because it showed larger amplitudes of oscillation when compared to the those observed when $H \parallel ab$. Measurements were performed in a reduced field range between 7 T and 3 T, using a small sweep rate of 10 Oe/s.

The molar magnetization M can be determined by dividing the magnetic moment measured in the MPMS by the number of mols n in the sample measured. Finally, the magnetic susceptibility χ is obtained by calculating the numerical derivative of the magnetization M relative to the applied magnetic field H .

4. RESULTS AND DISCUSSION

NiTe₂ single crystals were obtained in the hexagonal 1T-type structure, space group $P\bar{3}m1$. This material has layers of Te bounded by van der Waals interaction, classifying it as a 2D material (Fig. 6a). X-ray diffraction confirmed the correct phase was obtained, with cell parameters $a = b = 3.852(1)$ Å and $c = 5.266(3)$ Å. The $\chi^2 = 3.06$ is a representation of the quality of the sample obtained (Fig. 6b).

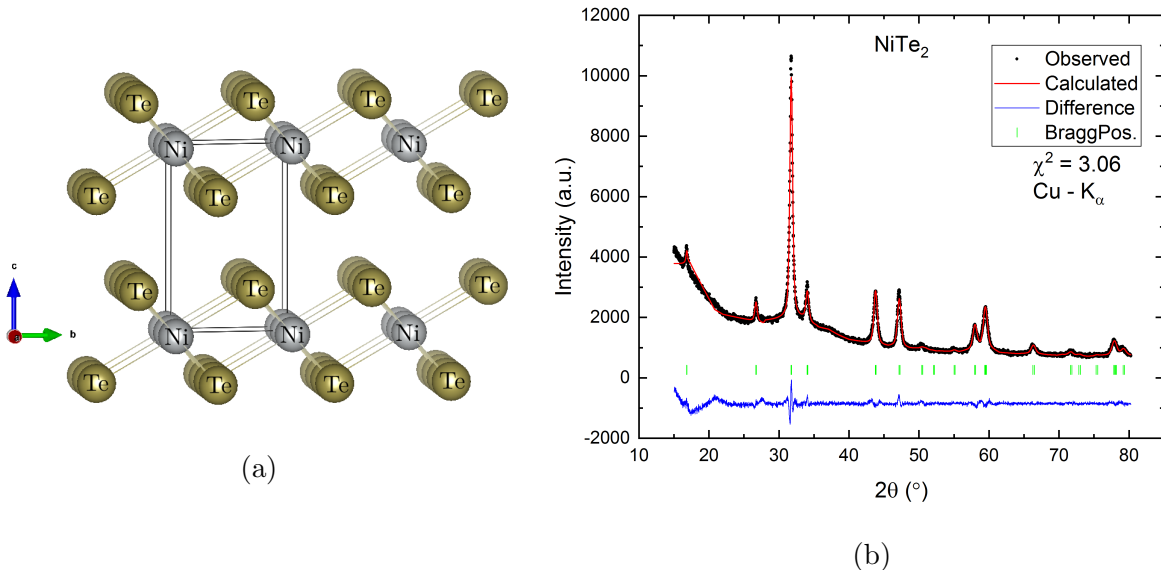


Figure 6: **(6a)** Unit cell of the 1T NiTe₂ structure, where the Te-Te planes can be seen stacked along the c-axis. **(6b)** Powder X-ray diffraction pattern of NiTe₂, with calculated pattern showing the correct phase was obtained. The χ^2 of 3.06 shows the quality of the refinement.

In Fig. 7a, the resistivity of NiTe₂ is shown and features a linear increase with temperature above ~ 50 K. This is typical behaviour in metals, where the disordered heat energy agitates the ions, which scatter the charge carriers in the Fermi liquid state, increasing the resistance.

By dividing the resistivity at $T = 300$ K by the value at zero temperature (or the lowest available temperature), the residual resistivity ratio (RRR) can be obtained. In the case of an ideal metal with no impurities to scatter the charge carriers, the resistance would vanish at 0 K and the RRR would be infinitely large, so experimentally large finite values are a sample quality indicator. In NiTe₂, the value of $RRR = 53.0$ is another indication of the

high quality of the single crystals obtained through the self-flux method.

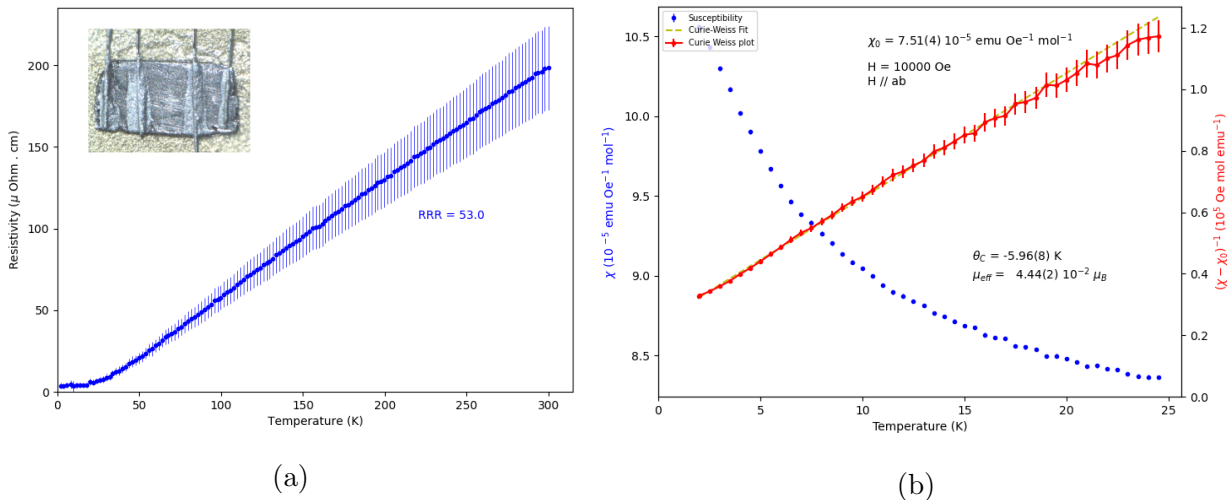


Figure 7: **(7a)** Resistivity of NiTe₂ showing a typical metallic behaviour, with a linear dependency on temperature and a residual resistivity ratio (RRR) of 53. The inset shows the sample measured with the four probe method. **(7b)** In blue, the susceptibility of NiTe₂ is shown, and in red, the data is plot according to the Curie-Weiss relation subtracting the constant Pauli paramagnetism (see main text). The measurement was taken with an applied field of 10 kOe, parallel to the *ab*-plane.

The magnetic moment of NiTe₂ showed a constant paramagnetic dependence from room temperature down to about 40 K. At low temperatures, the susceptibility was fitted considering the Curie-Weiss law, with a temperature-independent susceptibility χ_0 (Fig. 7b):

$$\chi = \frac{C}{T - T_c} + \chi_0, \quad (30)$$

where C is the Curie constant and T_c the Curie temperature.

Considering a microscopic theory of magnetism, the Curie-Weiss behaviour is derived from the magnetic moments and spins of the atoms in the lattice, where T_c represents the maximum temperature at which spontaneous magnetization occurs, and C is directly related to the magnetic moment of the system, through the relation:

$$C = \frac{\mu_0 N_A}{3k_B} \mu_{eff}^2 \Rightarrow \mu_{eff} \approx \sqrt{8C}, \quad (31)$$

where the approximation is done in CGS gaussian units, and the effective moment is given in Bohr magnetons (μ_B) [45]. An effective magnetic moment of $4.44(2) \times 10^{-2} \mu_B$ was found,

which is orders of magnitude smaller than in a regular paramagnet, therefore most likely comes from small amounts of impurities in the reagents.

The temperature independent susceptibility was found to be $\chi_0=7.51(4)\times 10^{-5}$ emu/mol, and we can analyze it to obtain an approximation for the density of states at the Fermi level (based on the analysis of Jiao *et al.* [46]). In general form, this value χ_0 is a composition of the Pauli paramagnetism (χ_p), Landau diamagnetism (χ_L), core diamagnetism (χ_c) and Van Vleck paramagnetism (χ_{vv}). Since NiTe₂ has metallic behaviour with low effective moment, the susceptibility observed will mainly come from itinerant electrons, meaning that the χ_{vv} can be disregarded when compared to χ_p . χ_L can be estimated as $\approx -\frac{1}{3}\chi_p$ by assuming the diamagnetism is not enhanced by electron-phonon interactions (reasonable at low temperatures). Finally, the core diamagnetism can be calculated directly as $\chi_c=-4\times 10^{-5}$ emu/mol from the tabled values of reference [47]. We then get $\chi_p=\frac{3}{2}(\chi_0 - \chi_c)=1.726\times 10^{-4}$ emu/mol, consistent to other topological semimetals. From this, we can obtain the density of states at the Fermi level η_F using the Pauli susceptibility expression from Fermi-liquid theory $\chi_P = \mu_B^2\eta_F$, resulting in $\eta_F = 5.15$ states/(eV f.u.).⁴

From the dependence of the magnetization with applied magnetic field for several different temperatures (inset Fig. 8a) it is possible to see the initial raw manifestation of the quantum oscillations originated from the dHvA effect. By subtracting a linear background and plotting the magnetization as a function of the inverse magnetic field (as suggest by Eq. 27), two summed periodic oscillations of different frequencies can clearly be seen in the main plot (Fig. 8a). The same data is shown separated by vertically shifting a fixed amount for the different temperatures (Fig. 8b) to facilitate visualization.

The next step is to calculate the Fast Fourier Transform (FFT) of this signal to obtain the frequency and amplitude of each oscillation, and quantitatively observe how it changes with temperature. Since FFT requires a linearly spaced x-axis, a Savitsky-Golay filter (cubic interpolation in a window of 7 data points) was used to interpolate and further reduce experimental noise. The resulting FFT (Fig. 9a) shows two clear peaks, labelled as F_α and F_β for the lower and higher frequency, respectively.

In order to retrieve information of the FFT peaks, a Lorentzian curve was fitted for each.

⁴ It is important to remember that the magnetic susceptibility (in emu/mol) is calculated dividing by the magnetic field in *cgs* units of G, so the Bohr magneton constant has to be taken considering 1 T = 10⁴ G before calculating the density of states.

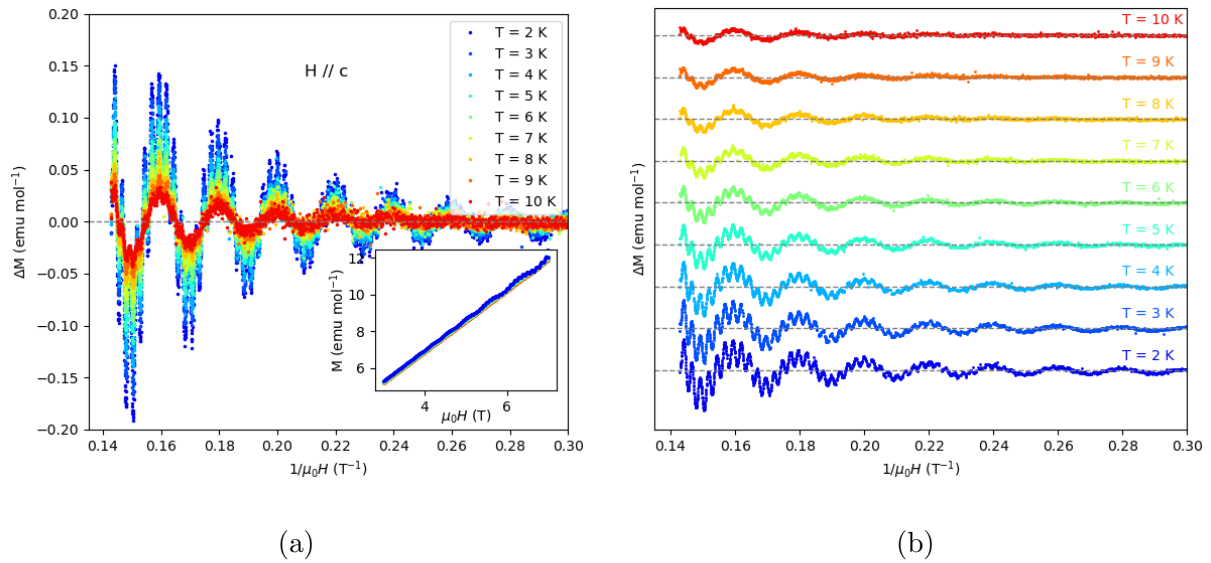


Figure 8: **(8a)** Background-subtracted magnetization as a function of the inverse magnetic field (dHvA plot). The inset shows the originally measured magnetization as a function of applied magnetic field. **(8b)** The same dHvA plot, but with each temperature curve displaced to facilitate visualization.

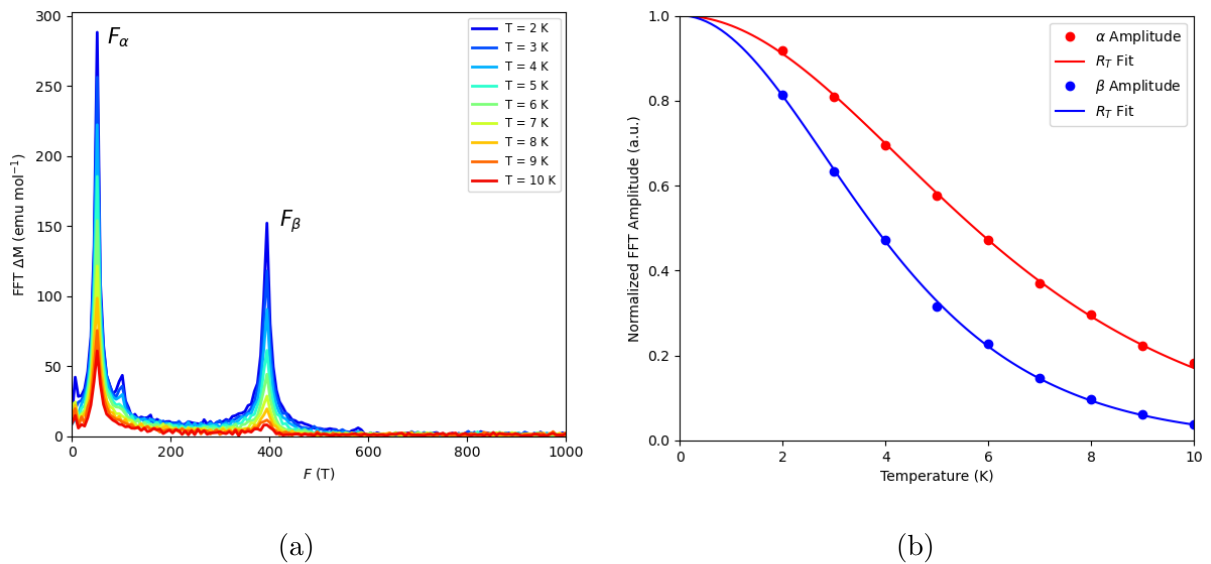


Figure 9: **(9a)** Fast Fourier Transform of the dHvA oscillations for all measured temperatures. **(9b)** Normalized amplitude of the FFT peak for each frequency, as a function of temperature.

The center gives the frequency of oscillation of $F_\alpha = 50.5(5)$ T ($F_\beta = 393.6(6)$ T) and, using Onsager's relation (Eq. 22), the Fermi surface area is determined to be $A_F^\alpha = 0.0767(9)$ nm⁻² ($A_F^\beta = 0.598(1)$ nm⁻²). The height of the peaks are temperature-dependent and have been plotted normalized to the extrapolated 0 K height (Fig. 9b). In the Lifshitz-Kosevich theory, this temperature dependence is uniquely defined by the R_T damping factor (Eq. 24), that fits very well the experimental data, giving an effective mass of $m_\alpha^* = 0.13(3)m_0$ ($m_\beta^* = 0.20(4)m_0$), where m_0 is the free electron mass⁵. These very low values are similar to the ones reported in literature [19, 48], and are justified from the carriers' relativistic properties expected from the linearly dispersing band structures shown in DFT calculations [19, 20, 48].

The scattering properties of the charge carriers can now be analyzed from the Dingle damping factor on the oscillation amplitudes. The first method used to determine the Dingle temperature T_D is by directly fitting the LK formula (Eq. 28) to the obtained signal. In our case, the two summed oscillations would result in too many fitting parameters, so we can further simplify by passing a band filter in the FFT, which consists of making the inverse Fourier transform in a frequency range only around the desired peak. This deconvolution procedure separates the two oscillations, and the result can be seen in Fig. 10a for the temperature of 2 K.

Now, the separate curves can be fitted using Eq. 28, where we can use the previously calculated value for the relative mass μ and obtain the Dingle temperature of $T_D^\alpha = 7.9(1.0)$ K ($T_D^\beta = 9.1(1.9)$ K), resulting in the relatively large quantum relaxation times of $\tau_q^\alpha = 0.15(4)$ ps ($\tau_q^\beta = 0.13(3)$ ps). The fitted oscillations can be summed up to show good agreement with the pure signal obtained at 2 K (Fig. 10b).

The second and more standard method to obtain the Dingle temperature is based on linearization of the LK formula. By determining absolute values of the maximum and minimum amplitudes of the deconvoluted oscillations ΔM_{Amp} , Eq. 28 can be rearranged to

$$\log\left(\frac{\Delta M_{Amp}}{B^{1/2}R_T}\right) = -\alpha T_D \mu \frac{1}{B} + \log(C), \quad (32)$$

where C is the proportionality constant in the LK formula. The resulting plot for the data obtained at 2 K is shown in Fig. 11a. From the angular coefficient of the linear regression,

⁵ The uncertainties are calculated in Appendix B, where the relatively large error for the mass is explained.

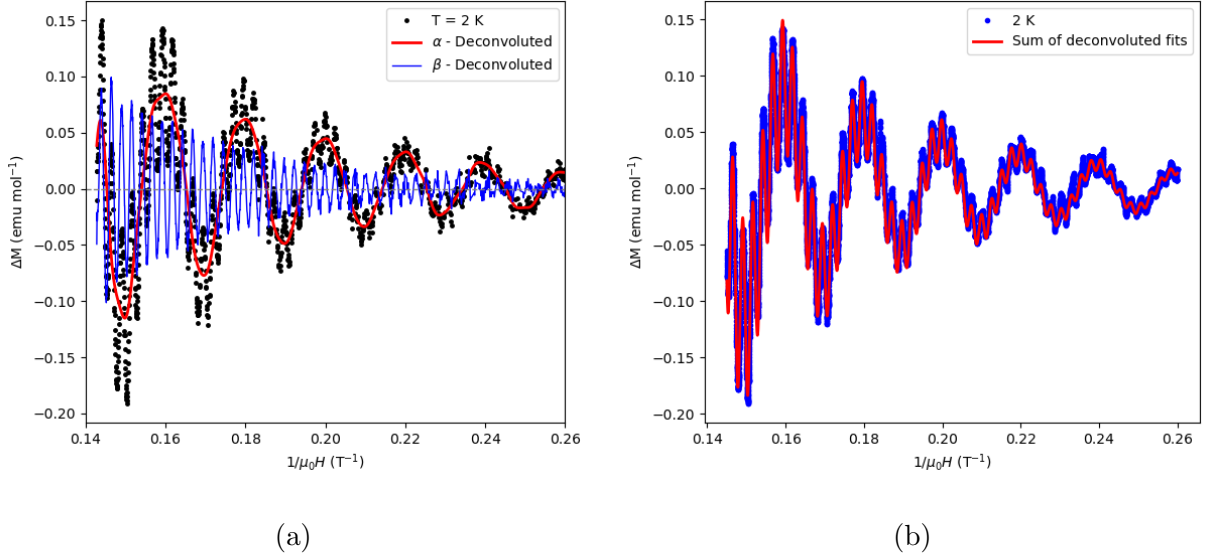


Figure 10: **(10a)** dHvA oscillations at 2 K before (in black) and after deconvoluting the frequencies through a band filter. **(10b)** Full dHvA oscillation fitted with the LK equation (Eq. 28). The fits were made in the deconvoluted frequencies, and later summed to obtain the curve seen here.

the Dingle temperature is determined to be $T_D^\alpha = 5.1(1.0)$ K ($T_D^\beta = 7.9(1.0)$ K), well in agreement with the values obtained through the previous method. All values, as well as the quantum relaxation times τ_q and the quantum mobilities μ_q obtained are reported in Table I.

Finally, the topological aspect of the Fermi surface can be probed by finding the Berry phase in the dHvA oscillations. The simplest method to find the oscillation phase, as in the case of the Dingle temperature, consists on fitting the LK formula (Eq. 28) in the deconvoluted frequencies. But the most standard way is by assigning integer (half-integer) indices to the maximum (minimum) of the magnetic susceptibility, in the so-called Landau Fan Diagram. First, consider the differential susceptibility $\Delta\chi = \frac{d(\Delta M)}{dB}$ as

$$\Delta\chi \propto \text{sign}(R_S) \cos \left[2\pi \left(\frac{F}{B} - \gamma + \delta \right) \right]. \quad (33)$$

Without considering the $\text{sign}(R_S)$, the maximum of such oscillation appears when the argument of the cosine function is an integer multiple of 2π , which gives the linear relation $N = F \frac{1}{B} - \gamma + \delta$. Notice that the angular coefficient is the frequency of oscillation, and the intercept is $-\gamma + \delta$. The integers must be displaced until $N(0) \in [-1, 1]$.

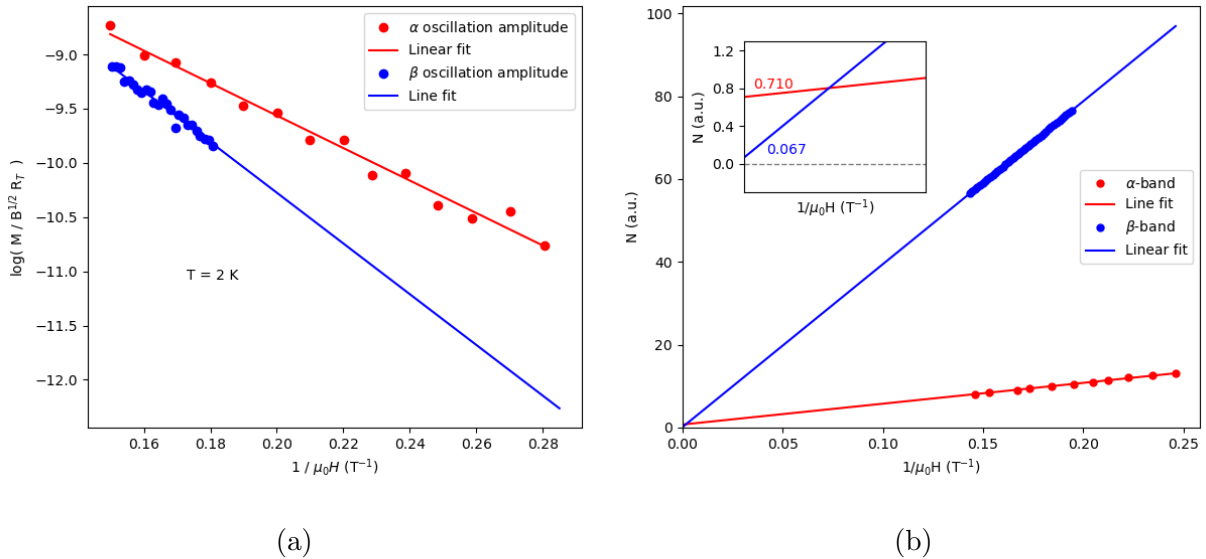


Figure 11: **(11a)** Linearization of the amplitude of oscillation through the Dingle plot, where T_D can be retrieved from the linear coefficient. **(10b)** Landau fan diagram, commonly used to find the phase of the oscillation. In the inset, the region close to 0 is zoomed in.

As suggested from Eq. 33, the sign of the spin reduction factor $R_S = \cos\left(\frac{\pi g \mu}{2}\right)$ is important in this case because it changes the phase by a factor of π , precisely the difference between a trivial and a topological material. So there is still a need to find the value of the Landé g -factor of the total angular momentum. As described in Session 2.2.3, R_S appears due to the splitting of the degenerate bands from the Zeeman effect. The simplest method to find g consists simply in applying a high magnetic field, making this splitting large enough to show a slight difference in the frequency of oscillation. An example where this is possible is for the nodal-line topological semimetal ZrSiS [49], where the g factor is found to have a large value of $g \approx 38$, but measurements in NiTe₂ up to 31 T show no such behaviour [48].

Alternatively, the spin-zero method used regularly in high- T_c cuprate superconductors and other quasi-2D materials, do not require a large Zeeman splitting, but is only completely accurate in a 2D Fermi surface. In this situation, the effective mass gets progressively heavier as the applied magnetic field gets tilted from the normal vector of the 2D-plane by an angle θ , following a relation of the form $\mu(\theta) = \mu(0)/\cos(\theta)$. Then, the argument inside R_S gets a dependence on the direction of the applied field, and one can determine g from the angle where the amplitude is null. An attempt to do this for NiTe₂ was performed by Zheng *et*

al. [48] but they found a large anisotropy with inconclusive results, a consequence of doing this analysis in a material with a 3D-FS.

Unfortunately, there is no other way to find the g factor from the dHvA oscillations, meaning the Berry phase determined here might be altered by π . Nevertheless, it is still possible to see if $\Phi_B \neq 0$, and conclude that the material is topologically non-trivial. The results for $R_S > 0$ are reported in Table I.

From theoretical band structure calculations [19, 48], the α -band dHvA oscillation comes from spherical-like hole pockets where only outer extremal areas are available to the cyclotron orbits. This means we expect $\delta = -1/8$ for α -band. Meanwhile, in the β -band, the Fermi surface looks like a distorted cylinder where both outer and inner extremal orbits are possible, but each with very different frequencies. Since the inner cyclotron orbits show a frequency value close to the F_β calculated in this work, and the outer area relates to a frequency higher than 1000 T, it is safe to assume the dHvA oscillation from this band comes from the inner orbit ($\delta = +1/8$). In Table I, the corresponding Berry phases are marked in bold.

Table I: Oscillation frequency (F), Fermi surface area (A_f), Dingle temperature (T_D), effective charge carrier mass (m^*/m_0), quantum lifetime (τ_q), quantum mobility (μ_q) and Berry phase (Φ_B) of NiTe₂ extracted by the de Haas-van Alphen oscillations analyses. The expected values for the dimension-dependent δ are marked in bold (see main text).

Band	F	A_f	T_D	m^*/m_0	τ_q	μ_q	Φ_B^a		
	(T)	(10 ⁻² nm ⁻²)	(K)		(ps)	(10 ³ cm ² V ⁻¹ s ⁻¹)	$\delta = -1/8$	$\delta = 0$	$\delta = +1/8$
α	50.5(5) ^b	7.67(9)	5.1(1.0) ^b		0.24(5)	3.16(92)	0.67(31) π^b	0.42(31) π^b	0.17(31) π^b
	50.08(1) ^c	7.609(1)	7.8(1.6) ^c	0.13(3)	0.15(6)	2.05(59)	0.75(1) π^c	0.50(1) π^c	0.25(1) π^c
β	393.6(6) ^b	59.8(1)	7.9(1.0) ^b		0.15(4)	1.34(39)	1.38(17) π^b	1.13(17) π^b	0.88(17) π^b
	393.82(1)	59.831(2)	9.1(1.9) ^c	0.20(4)	0.13(3)	1.16(34)	1.33(1) π^c	1.08(1) π^c	0.83(1) π^c

^a This assumes $R_S > 0$, for $R_S < 0$ sum π ; ^b F from the FFT peak frequency, T_D from the Dingle plot, and Φ_B from Landau fan diagram; ^c Calculated from fitting of LK formula to deconvoluted oscillation.

Using these theoretical results and the values calculated from fitting the LK formula to the oscillations, the Berry phase for the α -band is $\Phi_B^\alpha = 0.75(1)\pi$ in the case where $R_S^\alpha > 0$ and $\Phi_B^\alpha = -0.25(1)\pi$ when $R_S^\alpha < 0$. For the β -band oscillations, $\Phi_B^\beta = 0.83(1)\pi$ when $R_S^\beta > 0$ and $\Phi_B^\beta = -0.17(1)\pi$ when $R_S^\beta < 0$. Even though we cannot further select the

results, all of these have values differ from 0, meaning the dHvA oscillations in NiTe₂ come from topological bands and relativistic fermions.

5. CONCLUSIONS

Single crystals of the type-II Dirac semimetal NiTe₂ were grown through the self-flux method. Powder X-ray diffraction was used to confirm the correct hexagonal crystalline phase was achieved. The highly metallic character of the sample was observed through resistivity measurements and from the dominant Pauli paramagnetism of the itinerant electrons. A small antiferromagnetic signal was observed in the magnetization, but it is attributed to impurities in the reagent.

Most importantly, quantum mechanical oscillations on the magnetization enabled an indirect look at the Fermi surface of NiTe₂, through the de Haas-van Alphen effect. Two different frequencies of oscillations were resolved, each related to one band crossing the Fermi surface, showing relatively low scattering properties and relativistic effective masses of 0.13(3) m_0 and 0.20(4) m_0 . The band topology was determined to be non-trivial, even though the Berry phase could not be precisely obtained only through the dHvA effect analyses.

The work performed here is based on the paper by Xu *et al.* [19], but there are a few important differences: (I) the Berry phase determination was not performed correctly in the above cited paper (and most of current literature). The analysis here is performed considering remarks made by Hu *et al.* [49], Shen *et al.* [50] and Shoenberg [33]; (II) alternative explanation on the low antiferromagnetic signal, following the discussion by Zheng *et al.* [48]; (III) additional analysis on the Pauli paramagnetic susceptibility based on Jiao *et al.* [46].

Even though the experimental characterization of the Fermi surface through dHvA oscillations in pure NiTe₂ could not be further improved with respect to the results already in the literature⁶, some preliminary results in Se-doped NiTe₂ (not presented in this graduation thesis) showed that the dHvA oscillations are robust enough to survive the inevitable disorder introduced by Se. Since this substitution is expected to allow a certain level of tuning of the pristine material band structure, NiTe_{2-x}Se_x may present an ideal platform to

⁶ Zheng *et al.* performed a study in 2020 of the dHvA oscillations on NiTe₂ up to 31 T and with an angular dependence, mapping to the entire Fermi surface [48]

follow the evolution of the “Fermi surface” using the dHvA effect, and is planned as future work.

Appendix A: Some mathematical deductions

1. Getting the harmonic oscillator Hamiltonian

In our problem, Schrodinger's equation has the form

$$\frac{1}{2m} \left[\left(\hat{p}_x + \frac{eH\hat{y}}{c} \right)^2 + \hat{p}_y^2 + \hat{p}_z^2 \right] \psi + \frac{g_s\mu_B}{\hbar} s_z H \psi = \epsilon \psi. \quad (\text{A1})$$

Using the *ansatz* for the eigenfunction:

$$\psi = \chi(y) e^{\frac{i}{\hbar}(xp_x + zp_z)}, \quad (\text{A2})$$

and with the momentum operators in coordinate basis as $\hat{p}_y = -i\hbar \frac{d}{dy}$ and that $\hat{p}_{x,z}\psi = p_{x,z}\psi$, we can substitute back on Schrodinger's equation:

$$\frac{1}{2m} \left[p_x^2 \chi + 2 \left(\frac{eH\hat{y}}{c} \right) \chi p_x + \left(\frac{eH\hat{y}}{c} \right)^2 \chi - \hbar^2 \frac{d^2 \chi}{dy^2} + p_z^2 \chi \right] + \frac{g_s\mu_B}{\hbar} s_z H \chi = \epsilon \chi \quad (\text{A3})$$

which can then be simplified to

$$-\frac{\hbar^2}{2m} \chi'' + \frac{p_z^2}{2m} \chi + \frac{g_s\mu_B}{\hbar} s_z H \chi + \frac{1}{2m} \left[p_x^2 + 2 \left(\frac{eHy}{c} \right) p_x + \left(\frac{eHy}{c} \right)^2 \right] \chi = \epsilon \chi \quad (\text{A4})$$

and finally

$$\chi'' + \frac{2m}{\hbar^2} \left(\epsilon - \frac{g_s\mu_B}{\hbar} s_z H - \frac{p_z^2}{2m} - \frac{m}{2} \left(\frac{eH}{mc} \right)^2 \left[y - \left(-\frac{cp_x}{eH} \right) \right] \right) \chi = 0. \quad (\text{A5})$$

Now we can define the constants

$$\omega_H = \frac{eH}{mc}; \quad y_0 = \frac{-cp_x}{eH}, \quad (\text{A6})$$

resulting in

$$\chi'' + \frac{2m}{\hbar^2} \left[\epsilon - \frac{g_s\mu_B}{\hbar} s_z H - \frac{p_z^2}{2m} - \frac{1}{2} m \omega_H^2 (y - y_0) \right] \chi = 0, \quad (\text{A7})$$

which is the ODE for the quantum harmonic oscillator, with 2 extra terms that don't depend on y .

2. Calculating the energy

In this section, the detailed calculations of the system's energy are presented. From the single particle energy with no k_z

$$\epsilon = \hbar\omega_H \left(n + \frac{1}{2} + \sigma \right),$$

we sum over all $N = \eta(k + \lambda)$ electrons in each energy level:

$$E(H) = \eta\hbar\omega_H \left[\sum_{n=0}^{k-1} \left(n + \frac{1}{2} \right) + \left(k + \frac{1}{2} \right) \lambda \right] \quad (\text{A8})$$

$$= \eta\hbar\omega_H \left[k \left(\frac{k-1}{2} + \frac{1}{2} \right) + \left(k + \frac{1}{2} \right) \lambda \right] \quad (\text{A9})$$

$$= \eta\hbar\omega_H \left[\frac{k^2}{2} + \left(k + \frac{1}{2} \right) \lambda \right] \quad (\text{A10})$$

$$= \eta\hbar\omega_H \left[\frac{(k + \lambda)^2}{2} + \frac{\lambda - \lambda^2}{2} \right] \quad (\text{A11})$$

$$= N\hbar\omega_H \left[\frac{k + \lambda}{2} + \frac{\lambda(1 - \lambda)}{2(k + \lambda)} \right] \quad (\text{A12})$$

$$= \frac{N^2\hbar\omega_H}{2\eta} + \frac{N\hbar\omega_H}{2(k + \lambda)}\lambda(1 - \lambda), \quad (\text{A13})$$

and by considering that the cyclotron frequency $\omega_H = \frac{eH}{mc}$ and the degeneracy is $\eta = \frac{AH}{\phi_0} = \frac{2AHe}{hc}$, we obtain

$$E(H) = \frac{N^2\pi\hbar^2}{2mA} + \frac{N\hbar\omega_H}{2(k + \lambda)}\lambda(1 - \lambda). \quad (\text{A14})$$

Finally, we take the energy at null field and temperature as

$$E(H = 0) = N^2 \frac{\pi\hbar^2}{2mA}, \quad (\text{A15})$$

and with $H_0 = \frac{hcN}{2eA} = \frac{N\phi_0}{A}$, the energy can be represented in a much simpler form

$$\frac{E(H)}{E(H = 0)} = 1 + \left(\frac{H}{H_0} \right)^2 \lambda(1 - \lambda). \quad (\text{A16})$$

Appendix B: Calculating uncertainties

Here, the formulas for the error in the calculated quantities will be derived, using that for a function of n variables $f(x_1, \dots, x_n)$ the error is given by

$$\sigma_f^2 = \sum_i^n \left(\frac{\partial f}{\partial x_i} \sigma_{x_i} \right)^2.$$

First, for the Fermi surface area using the Onsager relation (Eq. 22) $A_f = \frac{2\pi e}{\hbar c} F$, we directly get

$$\sigma_{A_f} = \frac{2\pi e}{\hbar c} \sigma_F = A_f \frac{\sigma_F}{F}. \quad (\text{B1})$$

For the temperature damping factor, we fit (Eq. 24) and obtain the relative mass from the fitting parameter b as $\mu = \frac{bB}{\alpha}$. Here we want to find the relative mass μ , and the error comes from the fitting parameter b and the field range used in the FFT ($B = \frac{1}{2}[B_{min} + B_{max}]$).

From the standard deviation of mean, we get

$$\sigma_B = \sqrt{\frac{1}{6} \sqrt{(B_{min} - B)^2 + (B_{max} - B)^2}},$$

which returns a relatively high error for the effective field used to calculate the mass (about 1.5 T), and then

$$\sigma_\mu = \mu \sqrt{\left(\frac{\sigma_B}{B}\right)^2 + \left(\frac{\sigma_b}{b}\right)^2}. \quad (\text{B2})$$

Next, we calculate the error on the Dingle temperature, with the fitting parameter d as the decay used when fitting the full LK formula to the deconvoluted oscillations or the angular coefficient in the linear Dingle plot, we get

$$\sigma_{T_D} = T_D \sqrt{\left(\frac{\sigma_\mu}{\mu}\right)^2 + \left(\frac{\sigma_d}{d}\right)^2}. \quad (\text{B3})$$

In the same manner, the quantum lifetime $\tau_q = \hbar/2\pi k_B T_D$ and mobility $\mu_q = e\tau_q/m^*$ have the error as

$$\sigma_{\tau_q} = \tau_q \frac{\sigma_{T_D}}{T_D}; \quad \sigma_{\mu_q} = \mu_q \sqrt{\left(\frac{\sigma_{\tau_q}}{\tau_q}\right)^2 + \left(\frac{\sigma_{m^*}}{m^*}\right)^2}. \quad (\text{B4})$$

Finally, the Berry phase is determined as $\Phi_B = 2\pi(\phi - \delta + \frac{1}{4} \pm \frac{1}{4})$, where ϕ is the phase determined through the LK fit or the intercept in the Landau Fan Diagram, so the error is given by

$$\sigma_{\Phi_B} = 2\pi\sigma_\phi. \quad (\text{B5})$$

Acknowledgements

I would like to take this opportunity to express my sincere gratitude to all of those who enabled and supported me during my undergrad years. First, to my advisor Prof. Dr. Marcos A. Avila, whose invaluable scientific guidance, immeasurable patience and continuous support not only led a confused Engineering student in a path to become a physicist, but continuously teaches me how to be a good person and scientist. I can honestly say that if it wasn't for him, I wouldn't even know of my dream of becoming a researcher. To my fellow members of the GMQ group (Prof. Julian, Prof. Rettori, Prof. Leticie, Cesar, Kariny, Gustavo and Deisy), thank you so much for our fruitful discussions, being scientific or simply during our coffee breaks in the afternoon. To all the friends UFABC brought to my life, thank you so much for keeping me company during these hard years. You all brought new perspectives on my life and our philosophical discussions were instrumental in keeping my sanity, specially during this last year in the pandemic. For those I already bring from past decades, thank you so much for always having my back, supporting my weird life decisions and pushing me to my best Δ . I would also like to thank my girlfriend Carla, whose love and support was essential in this final stage of writing, and powered even further my desire to follow my dreams. Last but not least, I dedicate this work to all my family, for your lifelong support is what enabled me to make the decisions I did and what eventually allowed me to become who I am today.

References

- [1] K. S. Novoselov, A. K. Geim, S. V. Morozov, D. Jiang, M. I. Katsnelson, I. Grigorieva, S. Dubonos, and A. Firsov, *Nature* **438**, 197 (2005).
- [2] C. L. Kane and E. J. Mele, *Phys. Rev. Lett.* **95**, 226801 (2005).
- [3] C. L. Kane and E. J. Mele, *Phys. Rev. Lett.* **95**, 146802 (2005).
- [4] M. Z. Hasan and C. L. Kane, *Rev. Mod. Phys.* **82**, 3045 (2010).
- [5] B. A. Bernevig, T. L. Hughes, and S.-C. Zhang, *Science* **314**, 1757 (2006).
- [6] D. Hsieh, D. Qian, L. Wray, Y. Xia, Y. S. Hor, R. J. Cava, and M. Z. Hasan, *Nature* **452**, 970 (2008).
- [7] Y. Xia, D. Qian, D. Hsieh, L. Wray, A. Pal, H. Lin, A. Bansil, D. Grauer, Y. S. Hor, and R. J. Cava, *Nature physics* **5**, 398 (2009).
- [8] N. P. Armitage, E. J. Mele, and A. Vishwanath, *Rev. Mod. Phys.* **90**, 015001 (2018).
- [9] S.-M. Huang, S.-Y. Xu, I. Belopolski, C.-C. Lee, G. Chang, B. Wang, N. Alidoust, G. Bian, M. Neupane, and C. Zhang, *Nature Communications* **6**, 1 (2015).
- [10] Z. Liu, L. Yang, Y. Sun, T. Zhang, H. Peng, H. Yang, C. Chen, Y. f. Zhang, Y. Guo, and D. Prabhakaran, *Nature Materials* **15**, 27 (2016).
- [11] D. F. Liu, A. J. Liang, E. K. Liu, Q. N. Xu, Y. W. Li, C. Chen, D. Pei, W. J. Shi, S. K. Mo, P. Dudin, T. Kim, C. Cacho, G. Li, Y. Sun, L. X. Yang, Z. K. Liu, S. S. P. Parkin, C. Felser, and Y. L. Chen, *Science* **365**, 1282 (2019).
- [12] S. Borisenko, Q. Gibson, D. Evtushinsky, V. Zabolotnyy, B. Büchner, and R. J. Cava, *Phys. Rev. Lett.* **113**, 027603 (2014).
- [13] Z. Wang, Y. Sun, X.-Q. Chen, C. Franchini, G. Xu, H. Weng, X. Dai, and Z. Fang, *Phys. Rev. B* **85**, 195320 (2012).
- [14] A. A. Soluyanov, D. Gresch, Z. Wang, Q. Wu, M. Troyer, X. Dai, and B. A. Bernevig, *Nature* **527**, 495 (2015).
- [15] L. Huang, T. M. McCormick, M. Ochi, Z. Zhao, M.-T. Suzuki, R. Arita, Y. Wu, D. Mou, H. Cao, and J. Yan, *Nature Materials* **15**, 1155 (2016).
- [16] Y. Wu, D. Mou, N. H. Jo, K. Sun, L. Huang, S. L. Bud'ko, P. C. Canfield, and A. Kaminski,

- Phys. Rev. B* **94**, 121113 (2016).
- [17] H. Huang, S. Zhou, and W. Duan, *Phys. Rev. B* **94**, 121117 (2016).
- [18] Y. Li, Y. Xia, S. A. Ekañana, N. Kumar, J. Jiang, L. Yang, C. Chen, C. Liu, B. Yan, C. Felser, G. Li, Z. Liu, and Y. Chen, *Phys. Rev. Materials* **1**, 074202 (2017).
- [19] C. Xu, B. Li, W. Jiao, W. Zhou, B. Qian, R. Sankar, N. D. Zhigadlo, Y. Qi, D. Qian, F.-C. Chou, *et al.*, *Chemistry of Materials* **30**, 4823 (2018).
- [20] B. Ghosh, D. Mondal, C.-N. Kuo, C. S. Lue, J. Nayak, J. Fujii, I. Vobornik, A. Politano, and A. Agarwal, *Phys. Rev. B* **100**, 195134 (2019).
- [21] S. Mukherjee, S. W. Jung, S. F. Weber, C. Xu, D. Qian, X. Xu, P. K. Biswas, T. K. Kim, L. C. Chapon, and M. D. Watson, *Scientific Reports* **10**, 1 (2020).
- [22] F. Zheng, X.-B. Li, P. Tan, Y. Lin, L. Xiong, X. Chen, and J. Feng, *Phys. Rev. B* **101**, 100505 (2020).
- [23] J. Zhang and G. Q. Huang, *Journal of Physics: Condensed Matter* **32**, 205702 (2020).
- [24] T. Li, K. Wang, C. Xu, Q. Hou, H. Wu, J.-Y. Ge, S. Cao, J. Zhang, W. Ren, X. Xu, *et al.*, *arXiv preprint arXiv:1911.07173* (2019).
- [25] M. Mandal and R. P. Singh, *Journal of Physics: Condensed Matter* **33**, 135602 (2021).
- [26] B. de Lima, R. de Cassia, F. Santos, L. Correa, T. Grant, A. Manesco, G. Martins, L. Eleno, M. Torikachvili, and A. Machado, *Solid State Communications* **283**, 27 (2018).
- [27] Z. Feng, J. Si, T. Li, H. Dong, C. Xu, J. Yang, Z. Zhang, K. Wang, H. Wu, Q. Hou, J.-J. Xing, S. Wan, S. Li, W. Deng, J. Feng, A. Pal, F. Chen, S. Hu, J.-Y. Ge, C. Dong, S. Wang, W. Ren, S. Cao, Y. Liu, X. Xu, J. Zhang, B. Chen, and N.-C. Yeh, *Materials Today Physics* **17**, 100339 (2021).
- [28] W. De Haas and P. Van Alphen, *Proc. Netherlands Roy. Acad. Sci* **33**, 170 (1930).
- [29] L. Landau, *Zeitschrift für Physik* **64**, 629 (1930).
- [30] L. Landau and E. Lifshitz, *Quantum Mechanics: Non-relativistic Theory*, Course of theoretical physics (Pergamon Press, 1977).
- [31] L. Onsager, *The London, Edinburgh, and Dublin Philosophical Magazine and Journal of Science* **43**, 1006 (1952).
- [32] I. Lifshitz and A. Kosevich, *Sov. Phys. JETP* **2**, 636 (1956).
- [33] D. Shoenberg, *Magnetic Oscillations in Metals*, Arnold and Caroline Rose Monograph Series of the American Society (Cambridge University Press, 1984).

- [34] G. P. Mikitik and Y. V. Sharlai, *Phys. Rev. Lett.* **82**, 2147 (1999).
- [35] T. Champel and V. P. Mineev, *Philosophical Magazine B* **81**, 55 (2001).
- [36] Python Software Foundation, Python, v 3.8, <https://www.python.org/>, Last accessed on 2020-03-20.
- [37] NumPy Developers, Numpy package, <https://www.numpy.org/>, Last accessed on 2020-03-20.
- [38] The Matplotlib Development Team, Matplotlib package, <https://www.scipy.org/>, Last accessed on 2020-03-20.
- [39] SciPy Developers, Scipy package, <https://www.scipy.org/>, Last accessed on 2020-03-20.
- [40] ASM, Asm alloy phase diagram, <https://matdata.asminternational.org/apd/index.aspx>, Last accessed on 2020-03-20.
- [41] Thermo Fisher Scientific, Alfa aesar, <https://www.alfa.com/en/>, Last accessed on 2020-03-20.
- [42] U. Centrais Experimentais Multiusuário, Multiuser central at ufabc, <http://propes.ufabc.edu.br/cem/equipamentos-e-agendamento/>, Last accessed on 2020-03-20.
- [43] J. Rodríguez-Carvajal, *Physica B: Condensed Matter* **192**, 55 (1993).
- [44] X. Cui, Z. Feng, Y. Jin, Y. Cao, D. Deng, H. Chu, S. Cao, C. Dong, and J. Zhang, *Journal of Applied Crystallography* **48**, 1581 (2015).
- [45] P. Mohn, *Magnetism in the Solid State: An Introduction*, Springer Series in Solid-State Sciences (Springer Berlin Heidelberg, 2005).
- [46] W.-H. Jiao, X.-M. Xie, Y. Liu, X. Xu, B. Li, C.-Q. Xu, J.-Y. Liu, W. Zhou, Y.-K. Li, H.-Y. Yang, S. Jiang, Y. Luo, Z.-W. Zhu, and G.-H. Cao, *Phys. Rev. B* **102**, 075141 (2020).
- [47] G. A. Bain and J. F. Berry, *Journal of Chemical Education* **85**, 532 (2008).
- [48] W. Zheng, R. Schönemann, S. Mozaffari, Y.-C. Chiu, Z. B. Gorau, N. Aryal, E. Manousakis, T. M. Siegrist, K. Wei, and L. Balicas, *Phys. Rev. B* **102**, 125103 (2020).
- [49] J. Hu, Z. Tang, J. Liu, Y. Zhu, J. Wei, and Z. Mao, *Phys. Rev. B* **96**, 045127 (2017).
- [50] K.-W. Chen, X. Lian, Y. Lai, N. Aryal, Y.-C. Chiu, W. Lan, D. Graf, E. Manousakis, R. E. Baumbach, and L. Balicas, *Phys. Rev. Lett.* **120**, 206401 (2018).